Mon. Not. R. Astron. Soc. **000**, 1–16 (2014) Printed 21 March 2014 (MN LATEX style file v2.2)

Diffuse gas properties and stellar metallicities in cosmological simulations of disc galaxy formation

Federico Marinacci[1,2⋆], Rüdiger Pakmor[1], Volker Springel[1,2] and Christine M. Simpson[1]

[1] *Heidelberger Institut für Theoretische Studien, Schloss-Wolfsbrunnenweg 35, 69118 Heidelberg, Germany*
[2] *Zentrum für Astronomie der Universität Heidelberg, Astronomisches Recheninstitut, Mönchhofstr. 12-14, 69120 Heidelberg, Germany*

arXiv:1403.4934v1 [astro-ph.CO] 19 Mar 2014

21 March 2014

ABSTRACT

We analyse the properties of the circum-galactic medium and the relation between its metal content and that of the stars comprising the central galaxy in eight hydrodynamical 'zoom-in' simulations of disc galaxy formation. The simulations employ the moving-mesh code AREPO combined with a comprehensive model for the galaxy formation physics, and succeed in forming realistic late-type spirals in the set of 'Aquarius' initial conditions of Milky Way-sized haloes. Galactic winds significantly influence the morphology of the circum-galactic medium and induce bipolar features in the distribution of heavy elements. They also affect the thermodynamic properties of the circum-galactic gas by supplying an energy input that sustains its radiative losses. Although a significant fraction of the heavy elements are transferred from the central galaxy to the halo, and even beyond the virial radius, the overall stellar metallicity distribution is broadly consistent with observations, apart from an overestimate of the [O/Fe] ratio in our default runs, an effect that can however be rectified by an increase of the adopted SN type Ia rate. All our simulations have difficulty in producing stellar metallicity gradients of the same strength as observed in the Milky Way.

Key words: methods: numerical – galaxies: abundances – galaxies: evolution – galaxies: haloes – galaxies: spiral – stars: abundances

1 INTRODUCTION

On large scales, dark matter only cosmological simulations (such as the Millennium runs, Springel et al. 2005; Boylan-Kolchin et al. 2009) have been very successful in reproducing the observed clustering properties of matter in the Universe, and have been of decisive help in establishing the current ΛCDM cosmological paradigm. Numerical simulations have also become an important tool for studying how galaxies in the high-redshift and present-day Universe form and evolve. However, at galactic and sub-galactic scales, the general picture of galaxy formation is still fraught with uncertainty. Much of the current simulation work in the field is thus attempting to clarify the role of different physical processes operating on galactic and sub-galactic scales, as well as their interplay within the cosmological context.

A major difficulty in galaxy formation simulations is posed by the intrinsic multi-scale and multi-physics nature of the problem. In fact, baryonic physics must be properly taken into account in addition to gravity if one wants to obtain a realistic description of galaxy formation and evolution. Unfortunately, important physical processes acting on baryons (e.g. AGN accretion) operate on spatial and temporal scales that are very much smaller than those of the galaxy as a whole, but they nevertheless play a fundamental role in shaping the global galactic features. It is this disparity of scales, together with the uncertainties in our understanding of the baryonic physics involved, that makes galaxy formation such a challenging problem.

To overcome these difficulties, a heuristic parametrization of the most important physical mechanisms for the galaxy formation process is frequently adopted (see Vogelsberger et al. 2013, and references therein). Recently, significant efforts have also been made to develop models that try to self-consistently include more of the relevant physical processes and hence to push back the use of ad hoc prescriptions to ever smaller scales (Hopkins et al. 2011, 2013; Renaud et al. 2013). Treating much of the baryon physics of star formation and associated feedback as 'subgrid' is however still the most widely used approach in the field and it is inevitable in large cosmological boxes for computational reasons. It has allowed significant advances in our under-

⋆ E-mail: federico.marinacci@h-its.org

© 2014 RAS

standing of galaxy formation by identifying the most relevant physical processes and isolating their role in determining the observed galaxy properties.

In particular, substantial progress has been made for what concerns the formation of late-type disc galaxies similar to the Milky Way (Agertz et al. 2011; Brooks et al. 2011; Guedes et al. 2011; Aumer et al. 2013; Stinson et al. 2013; Marinacci et al. 2014). For decades, this has been a sore point in the context of the ΛCDM cosmology because the galaxies predicted by the simulations were at odds with what was observationally known. The primary cause of these discrepancies lies in the so-called *overcooling* problem (Balogh et al. 2001): baryons at the centres of the dark matter haloes that host galaxies cool efficiently through radiative processes on a very short time scale, invariably leading to the formation of overly massive and overly concentrated galaxies (e.g. Abadi et al. 2003; Scannapieco et al. 2008, 2009; Stinson et al. 2010).

Therefore, realistic late-type galaxies can only be formed in simulations when the gas is supplied with an adequate amount of energy capable of partly offsetting its fast cooling rate and curtailing the production of stars. The source of this energy ultimately lies in the back-reaction that the star formation process (and also AGN accretion) exerts on the gas. Several channels (e.g. radiative, thermal, kinetic) are in principle conceivable to couple this energy to the cooling gas, with their relative importance still being debated (e.g. Sales et al. 2014). Different authors agree, however, that the adoption of very strong feedback physics lies at the heart of recent successful simulations of the formation of spiral galaxies (Guedes et al. 2011; Aumer et al. 2013; Stinson et al. 2013; Marinacci et al. 2014).

Independently of the detailed mechanism responsible for the efficient coupling of feedback energy to the star-forming gas, strong stellar feedback is expected to drive galactic-scale winds that expel metal-enriched gas out of the star-forming disc, possibly to distances comparable to or beyond the virial radius of the enclosing dark matter halo. This theoretical expectation appears to be confirmed by observations of star-forming galaxies at high- and low-redshift, showing that outflows from the sites of star formation to the circum-galactic medium (CGM) are a common phenomenon (Pettini et al. 2000; Strickland & Stevens 2000; Martin et al. 2002; Strickland et al. 2004; Soto et al. 2012).

Simulations suggest that the ejection of metal-enriched gas from galaxies to their haloes via galactic winds has at least two important consequences for galactic evolution. First, the ejected gas is (at least temporarily) unavailable for star formation, thereby preventing its rapid conversion into stars and alleviating the problem of forming overly massive bulge-dominated galaxies. Much of the ejected gas remains however bound to the galaxy's dark matter halo and thus can be re-accreted, providing fuel for late-time star formation that progressively builds up the disc (Scannapieco et al. 2012).

Second, wind material is more metal-rich with respect to the diffuse circum-galactic gas, and therefore represents an important source of metals for this gas component. Besides affecting its chemical composition, the interaction of the wind with the CGM can also significantly alter the dynamical and thermodynamical state of the diffuse gas. As we mentioned above, the mixture of wind material and circum-galactic gas provides fuel for late-time star formation. Therefore, galactic outflows also have an important influence on the properties of stars (in particular their metallicities), which in turn are responsible for wind generation. Since the wind strength in our parametrization of the galaxy formation physics has been set to reproduce the expected stellar mass, the properties of the CGM offer an important and powerful opportunity to check the consistency of the model.

In this paper we thus aim at investigating how the galactic-scale outflows contained in the simulations of Marinacci et al. (2014, hereafter MPS14) affect the features of the GCM surrounding late-type galaxies and those of the stars that they contain. To this end, we examine the properties of these two components, focusing in particular on their metal content, in a suite of eight hydrodynamical simulations of disc galaxy formation in Milky Way-sized haloes carried out with the moving-mesh code AREPO (Springel 2010). The simulation set has been previously introduced in MPS14, where we analysed the stellar mass distribution of the simulated galaxies, showing that our numerical methodology produces realistic disc galaxies that agree well with the observed scaling relations of late-type galaxies.

The paper is structured as follows. In Section 2, we summarize the salient characteristics of our simulation set and those of the numerical techniques that we used to perform the runs. We present the results of our analysis in Section 3 separately for gas (Sec. 3.1) and stellar (Sec. 3.2) properties. Finally, we discuss our findings in Section 4 and draw our conclusions in Section 5.

2 THE SIMULATION SET

We analyse a sub-set of the cosmological simulations of disc galaxy formation discussed in MPS14. These simulations can be viewed as hydrodynamical counterparts of the dark matter only simulations carried out in the Aquarius project (Springel et al. 2008), and include eight haloes (labeled Aq-A, Aq-B, etc., until Aq-H) selected to have a final total mass in a small range around $\sim 10^{12}\,\mathrm{M}_{\odot}$, comparable to recent determinations of the mass of the Galaxy (Sakamoto et al. 2003; Battaglia et al. 2005; Dehnen et al. 2006; Xue et al. 2008; Li & White 2008; Boylan-Kolchin et al. 2013). In addition to the mass selection criterion, the Aquarius haloes were chosen to have a relatively quiet merger history by enforcing a moderate isolation criterion, which favours the formation of extended, star-forming discs. More details about the selection criteria and the properties of these haloes can be found in the original Aquarius paper (Springel et al. 2008) and in Boylan-Kolchin et al. (2010).

The Aquarius simulation suite uses the so-called "zoom-in" technique to follow the formation of a target halo with much higher resolution than achievable in a homogeneously sampled cosmological box. In practice, the Lagrangian region that will collapse to form the central structure is discretized with a high number of low mass particles surrounded by several layers of progressively more massive particles that fill the total simulation volume. The masses of these low resolution particles increase with distance from the central object, such that the regions further away from the high-resolution volume are sampled more coarsely but still

sufficiently well to ensure an accurate accounting of all tidal forces acting on the target halo. This saves computational time without sacrificing the accuracy of the calculation.

In this paper we only analyse a single resolution level which is denoted as level '5', following the naming scheme of the Aquarius project. This also corresponds to the default resolution of the simulations presented in MPS14. The main properties of this resolution level[1] are a characteristic baryonic mass resolution of $\simeq 4.1 \times 10^5\,\mathrm{M}_\odot$, a dark matter mass resolution of $\simeq 2.2 \times 10^6\,\mathrm{M}_\odot$ and a maximum gravitational softening length at $z \leq 1$ of 680 pc in physical units for all mass components (dark matter and baryons) in the high-resolution region. In comoving units, the softening length is kept fixed for $z > 1$ in the high-resolution region and its physical counterpart is thus growing until $z = 1$, where it reaches the maximum allowed value and is then held fixed. Common to all the resolution levels in the Aquarius suite are a periodic box of $100\,h^{-1}$Mpc on a side and a ΛCDM cosmology with parameters $\Omega_\mathrm{m} = 0.25$, $\Omega_\mathrm{b} = 0.04$, $\Omega_\Lambda = 0.75$, $\sigma_8 = 0.9$, $n_\mathrm{s} = 1$ and a Hubble parameter $H_0 = 73$ km s^{-1}Mpc^{-1} (hence implying $h = 0.73$). This set of cosmological parameters is the same that has been used in the Millennium and Millenium-II simulations (Springel et al. 2005; Boylan-Kolchin et al. 2009).

To include gas in the original Aquarius initial conditions, we split each original dark matter particle, regardless of whether it is located in the high- or low-resolution region, into a pair composed of a dark matter particle and a gas cell, so that the whole simulation volume is filled with gas. We note that this differs from many studies performed with the SPH technique (e.g., Stinson et al. 2010; Guedes et al. 2011) where gas is often added to the high-resolution region only, causing a pressure discontinuity at the transition between the high- and low-resolution regions. The mass ratio in each dark matter particle-gas cell pair is set by the cosmic baryon mass fraction, while their positions and velocities are assigned by requiring that the centre-of-mass and the centre-of-mass velocity of the pair are preserved. This is done by displacing the dark matter and cell distributions such that two interleaved particle distributions are formed that are locally shifted relative to each other by half of the original mean inter-particle spacing.

We evolve the initial conditions with the moving-mesh cosmological code AREPO (Springel 2010). This code solves the gravitational and collision-less dynamics by using the same TreePM approach employed in the popular SPH code GADGET (Springel 2005). For what concerns the hydrodynamic part, AREPO solves Euler's equations on an unstructured Voronoi mesh by adopting a finite-volume discretization. The flux exchanges between cells are computed via a second-order MUSCL-Hancock scheme (e.g., Toro 1999) coupled to an exact Riemann solver. The special trait of AREPO compared to Eulerian grid-based codes is that the set of points generating its unstructured Voronoi mesh are allowed to freely move, and this additional degree of freedom is usually exploited by moving the mesh-generating points with the local fluid velocity. This causes a transformation of the mesh that adapts itself to the characteristics of the flow, giving rise to a quasi-Lagrangian numerical method which is manifestly Galilean-invariant and keeps the mass of each gas cell approximately constant. Further details about the code structure can be found in Springel (2010), while a detailed comparison between the moving-mesh approach and the smoothed particle hydrodynamics technique is presented in the tests performed by Vogelsberger et al. (2012) and Sijacki et al. (2012). Extensions of the basic method to include ideal magnetohydrodynamics have also been developed (Pakmor & Springel 2013) and applied successfully in cosmological simulations (Pakmor et al. 2014).

The present set of simulations uses a comprehensive model for galaxy formation physics (Vogelsberger et al. 2013) that implements the most important baryonic processes. The model has been specifically developed for the AREPO code and was calibrated to reproduce a small set of key observational findings for the global galaxy population (among others, the cosmic star formation history and the galaxy stellar mass function). The full description of the implementation is given in Vogelsberger et al. (2013) to which we also refer for a discussion of the predicted galaxy properties at $z = 0$ (see also Torrey et al. 2014, for an analysis of these properties at high redshift). Among the primary features of the model are:

(i) primordial and metal cooling rates including self-shielding corrections by Rahmati et al. (2013);

(ii) a variation of the Springel & Hernquist (2003) sub-resolution model for the ISM with the adoption of a Chabrier (2003) initial mass function;

(iii) a self-consistent treatment of stellar evolution, mass return from stars and metal enrichment (tracking H, He, C, N, O, Ne, Mg, Si, Fe and total metallicity) of the gas phase;

(iv) galactic winds implemented via a kinetic wind scheme, with mass loading computed according to an energy-driven scaling (see Puchwein & Springel 2013);

(v) wind metal loading offset with respect to the mass loading, necessary to reproduce the oxygen abundance of low mass haloes;

(vi) BH accretion and feedback based on a modification of the Springel et al. (2005) model, accounting for quasar, radio and radiative feedback channels;

(vii) a spatially uniform UV ionizing background (Faucher-Giguère et al. 2009);

(viii) a new Monte-Carlo formalism for Lagrangian tracer particles (Genel et al. 2013).

We use the same fiducial settings as in Vogelsberger et al. (2013) for the free parameters of the galaxy formation model, except for two minor modifications in the wind implementation and the radio-mode feedback of the BH module, respectively. These modifications are the same as in MPS14 and consist of providing the wind with some thermal energy in addition its kinetic energy, and adopting a more continuous heating model for the radio-mode feedback (see MPS14 for further discussion).

[1] The quoted mass resolution only applies exactly to the Aq-C halo. There are slight differences for the other haloes of the simulation set, within a factor of 2. The detailed list of properties for all the haloes can be found in Table 1 of MPS14.

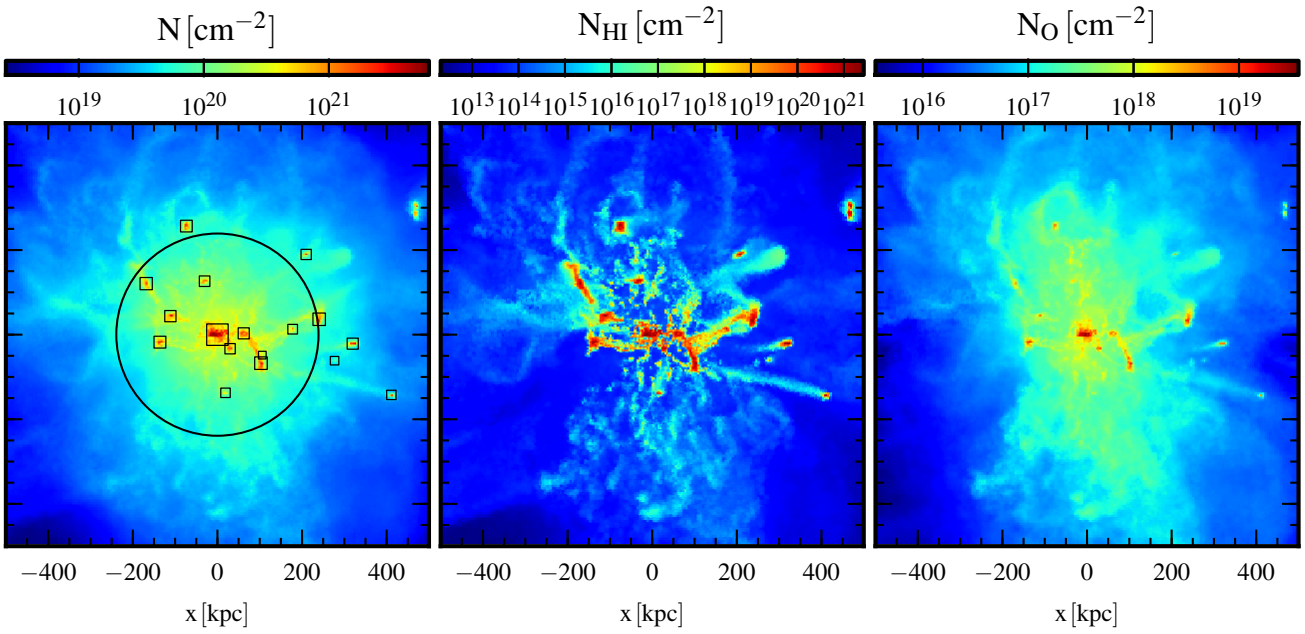

Figure 1. Column density maps of different chemical species for the Aq-A-5 simulation at $z = 0$. To compute the column density only the diffuse gas (i.e., non star-forming gas cells) has been taken into account. In the figure, the halo is oriented such that the central galaxy is seen edge-on to assess the impact of the adopted galactic wind model on the morphology and the metal enrichment of the CGM. To create the maps no cut in systemic velocity has been applied, but only the gas with a distance along the line of sight smaller than 500 kpc relative to the centre of the halo has been considered. In the leftmost panel, the black circle marks the position of the halo virial radius ($R_{\rm vir} = 239$ kpc), whilst the squares are centred on positions of the main galaxy and of satellites containing gas. Their sizes are scaled according to the gas mass.

3 RESULTS

3.1 Diffuse gas properties

Before starting the analysis of the features of the diffuse circum-galactic gas, we must define how we select this gas component in the simulations. In the context of our ISM treatment, we consider as diffuse gas all the gas cells whose density is below the star formation density threshold ($n_{\rm th} \simeq 0.13$ cm^{-3} for the fiducial setting adopted in the simulations). We note that this is a rather broad selection criterion since it encompasses relatively dense ($n \sim 0.1$ cm^{-3}) and cold ($T \sim 10^4$ K) gas in the immediate proximity and of the main galaxy (and satellites) as well as more tenuous ($n \sim 10^{-5}$ cm^{-3}) and hotter ($T \sim T_{\rm vir}$) gas phase that is expected to be distributed in the CGM on scales of ~ 100 kpc. The properties of the phases comprising this gas component are the topic of this section.

In Fig. 1, we present column density maps at $z = 0$ of the diffuse gas for the case of the simulation Aq-A-5. The total column density is shown together with the column densities of H I and oxygen to study both the large-scale morphology and the degree of chemical enrichment of the CGM. To create the maps, we choose a projection plane centered on the halo potential minimum, with a size of 1 Mpc on a side. We project all the gas cells that have a distance along the line of sight smaller than 500 kpc from the halo centre. We thus used a purely spatial selection criterion for the projections, although it is also possible to associate the diffuse gas to the halo based on kinematic information (Stinson et al. 2012). The latter method is what is actually adopted in absorption studies of the CGM both in the Milky Way (Sembach et al. 2003; Savage et al. 2003; Lehner et al. 2012) and in external galaxies (e.g., Prochaska et al. 2011) because of the lack of spatial information along the line of sight about the absorbers. However, we explicitly checked that our results do not strongly depend on the way the association between the halo and its CGM is made. For instance, adopting a cut in systemic velocity $|\delta v| = 200$ km s^{-1} produces results nearly indistinguishable from those presented in Fig. 1. Significant differences appear only if a rather extreme cut $|\delta v| < 50$ km s^{-1} is used. In the projections the halo is oriented such that the central galaxy would be seen edge-on. In other words, this means that the vertical axis on the maps is aligned with the galaxy symmetry axis, calculated according to the procedure described in MPS14. We choose that particular orientation because it is the most suited to show the effects of our galactic wind implementation – which is launched preferentially perpendicularly to the disc – on the structure of the CGM.

The total column density (left panel) of the CGM exhibits a very regular global morphology and extends in an almost spherical fashion slightly beyond the virial radius of the halo (the black circle in Fig. 1), where a more filamentary structure can be seen. Regions of gas with column densities in excess of 10^{21} cm^{-2} are usually compact and associated with the central galaxy and its satellites (indicated by black squares). This is also confirmed by the H I column density map (central panel), that shows indeed that the vast majority of the high column density gas is accounted for almost completely by this component. The H I morphology is

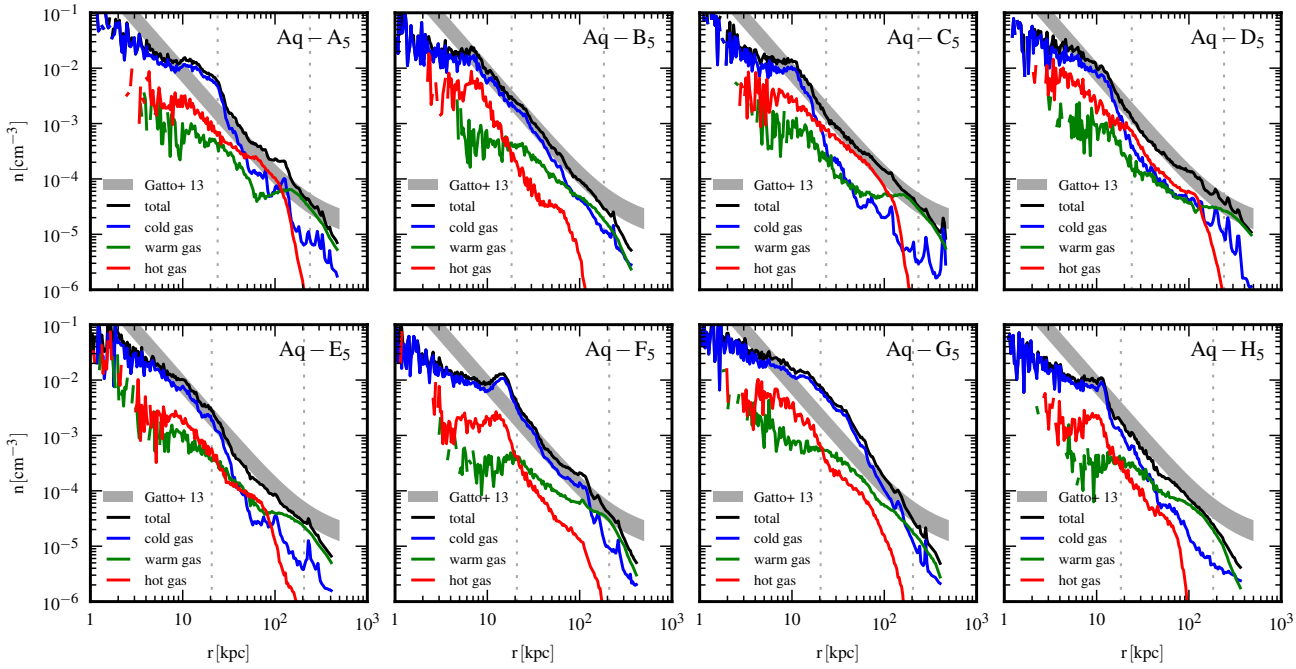

Figure 2. Spherically-averaged density profiles of the diffuse gas as a function of radius for the whole simulation set at $z = 0$. The diffuse gas has been divided into a cold phase (blue line) with $T < 10^5$ K, a warm phase (green line) with 10^5 K $< T < 10^6$ K and a hot phase with $T > 10^6$ K. The total density profile is indicated by the solid black line, while the dotted vertical lines are located at $0.1 \times R_{\rm vir}$ and $R_{\rm vir}$, respectively. The gray bands in all panels show the density range of an isothermal ($T = 1.8 \times 10^6$ K) model for the Milky Way's corona derived from ram pressure stripping simulations by Gatto et al. (2013).

much less regular and less extended with respect to the total column density. The neutral hydrogen tends to be preferentially located close to density peaks (i.e., in the vicinity of the central galaxy and its satellites) and drops by several orders of magnitude in between them. This cold material can be thought of as forming an interface between the star forming region of a galaxy and its environment, possibly mediating further cooling of hotter gas and thus feeding star formation (Marinacci et al. 2010, 2011).

The spatial distribution of heavy elements is similar for all the metal species that we track in our galaxy formation implementation. In the right panel of Fig. 1, we take oxygen as an example. It can be seen that the distribution of this element is markedly different from that of the H I and in fact it resembles more closely that of the total gas. Even in this case oxygen (and the other metals as well) is present up to and also beyond the virial radius of the halo. The presence of oxygen in these regions implies that galactic winds are very effective in ejecting metals from their production sites, i.e. the star forming regions of the (central) galaxy, to the surrounding environment. The fact that galactic winds are the main agent that causes metal enrichment of the CGM is also indicated by the morphology of the oxygen enriched region. As mentioned above, it looks smoother than the H I distribution and similar to the total gas column density but, compared to the latter, it is more elongated in the vertical direction, which is the preferred direction of wind ejection in our implementation. The wind – which is ultimately powered by supernovae associated with star formation – is more effective in ejecting metal-enriched material in the more active star-forming regions, such as those corresponding to the central galaxy, as can be seen from filaments with column density $\sim 10^{18}$cm^{-2} emanating from the centre and reaching heights of $\sim 100 - 150$ kpc.

In Fig. 2, we show spherically-averaged density profiles of the diffuse gas as a function of radius for the full simulated set of haloes at $z = 0$. The diffuse gas has been divided into three phases according to its temperature: a cold phase (blue lines) with $T < 10^5$ K, a warm phase (green lines) with 10^5 K $< T < 10^6$ K and a hot phase (red lines) with $T > 10^6$ K. The total gas density is indicated by the solid black line. Each profile has been derived by dividing the radial distance in 100 equally spaced logarithmic bins and then computing the gas mass falling into each bin. The average density then simply follows by dividing the bin mass by the volume of the spherical shell defined by each radial bin. Each halo generally features declining density profiles. The decreasing trend is somewhat less pronounced in the region within $0.1 \times R_{\rm vir}$, which is marked by the first of the two vertical dotted lines in the Fig. 2 (the other marking the location of the virial radius) and roughly coincides with the extension of the star-forming disc[2], and then becomes steeper from that point on out to the virial radius. The density profiles are dominated in the inner region by the cold phase. This seems to be the general trend also at larger radii with the noteworthy exceptions of the Aq-A and Aq-C haloes where it is the hot phase that gives the dominant contribution. Some other haloes (Aq-D and Aq-E), instead,

[2] We recall that this radial cut was used in MPS14 to select the material belonging to the central galaxy.

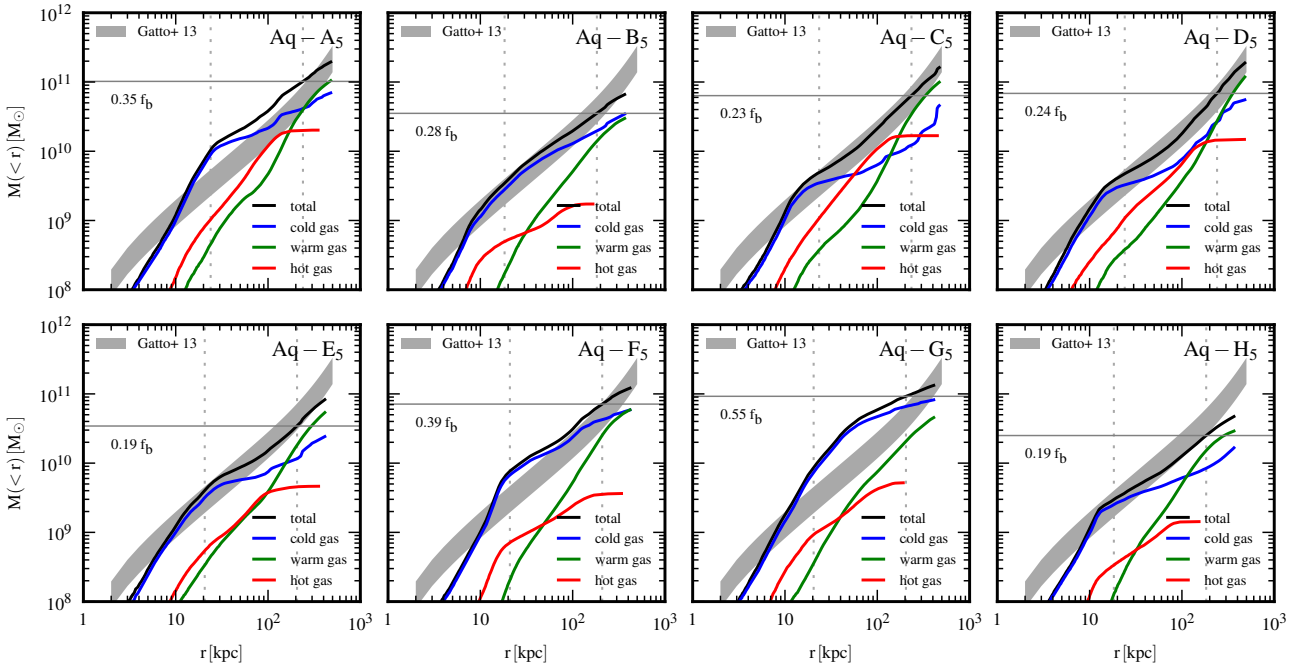

Figure 3. Cumulative mass profiles of the diffuse gas as a function of radius for the whole simulation set at $z = 0$. The contributions to the total mass of different gas phases, separated according to the gas temperature as in Fig. 2, are also plotted. The thin horizontal line in each panel shows the total mass in diffuse gas contained within the virial radius together with the indication of how this mass compares to that inferred from the universal baryon fraction. The gray bands in all panels indicate the allowed range of cumulative mass profiles of the Milky Way's corona model presented in Fig. 2.

show a roughly equal contribution to the total density of all three phases.

We compare our density profiles to those of an isothermal model for the Milky Way's corona derived from ram pressure stripping simulations of the dwarf spheroidal galaxies Sextans and Carina (Gatto et al. 2013). The allowed density range of the coronal model is shown by the gray bands in Fig. 2 and is consistent with the predictions of our simulations. However, we must stress that the match is excellent for our *total* density profiles, while in the simulations of Gatto et al. (2013) the corona is assumed to be composed of hot gas ($T = 1.8 \times 10^6$ K in the model shown here) close to the virial temperature of the Milky Way halo. As we have discussed above, the contribution of the hot gas to our density profiles is in general sub-dominant with respect to the cold gas. Only in the Aq-A and Aq-C haloes the density of the hot gas phase agrees with the ram pressure stripping constraints derived by Gatto et al. (2013).

Being the dominant phase in terms of density, it is not surprising that most of the mass of the diffuse gas in the simulations is contained in the cold phase. This is shown in Fig. 3, which presents cumulative mass profiles for the three phases defined above. The profiles are computed by ordering the gas cells according to their distance from the halo centre and summing their masses up to a given radius r. The thin horizontal line in each panel represents the total mass in diffuse gas inside the virial radius, and for each system we also report how this quantity compares to the total baryonic mass of the halo as inferred from the universal baryon fraction. Usually, the mass fraction contained in the diffuse gas is not negligible, ranging from $\sim 20\%$ to $\sim 40\%$ of the total baryonic mass in the halo predicted by cosmology, but not dominant either, since only in the case of the Aq-G halo it accounts for about the 55% of the total mass. As mentioned above, most of the mass is contained in the cold phase that shows a rapidly growing profile in the inner 20 kpc (which approximately corresponds to $0.1 \times R_{\rm vir}$ of the haloes) with a tendency of becoming flatter in the outer regions out to the virial radius. This flattening is always present but can sometimes be more pronounced depending on the relative contribution to the total mass of the warm and hot phases; the most extreme case being the Aq-C halo. For what concerns the (cumulative) mass profiles of the warm and hot phases they present the same trend in the inner regions of the cold counterpart (i.e., a rapid growth) but the mass of the warm gas continues to steadily increase up to the halo virial radius, while the mass of hot gas shows a flattening that is also found in the cold phase. The flatter trend starts at approximately the same radius as that of the cold gas in half of the haloes (Aq-B, Aq-F, Aq-G and Aq-H), while in the others this occurs beyond 100 kpc. A comparison of our results with those of Gatto et al. (2013) yields again an excellent agreement with respect to the total mass profiles, with values of the enclosed masses within the virial radius that are fairly similar in both cases. It is very encouraging that the two types of simulations reach consistent conclusions for the properties of the circum-galactic gas although they study different phenomena and also differ in the adopted numerical methodology.

To assess the degree of metal enrichment of the diffuse gas phase as a function of the distance from the central galaxy, we display in Fig. 4 two-dimensional histograms obtained by sampling the log Z − log r plane in 60×60 equally spaced bins for all the simulated haloes. The gray-scale en-

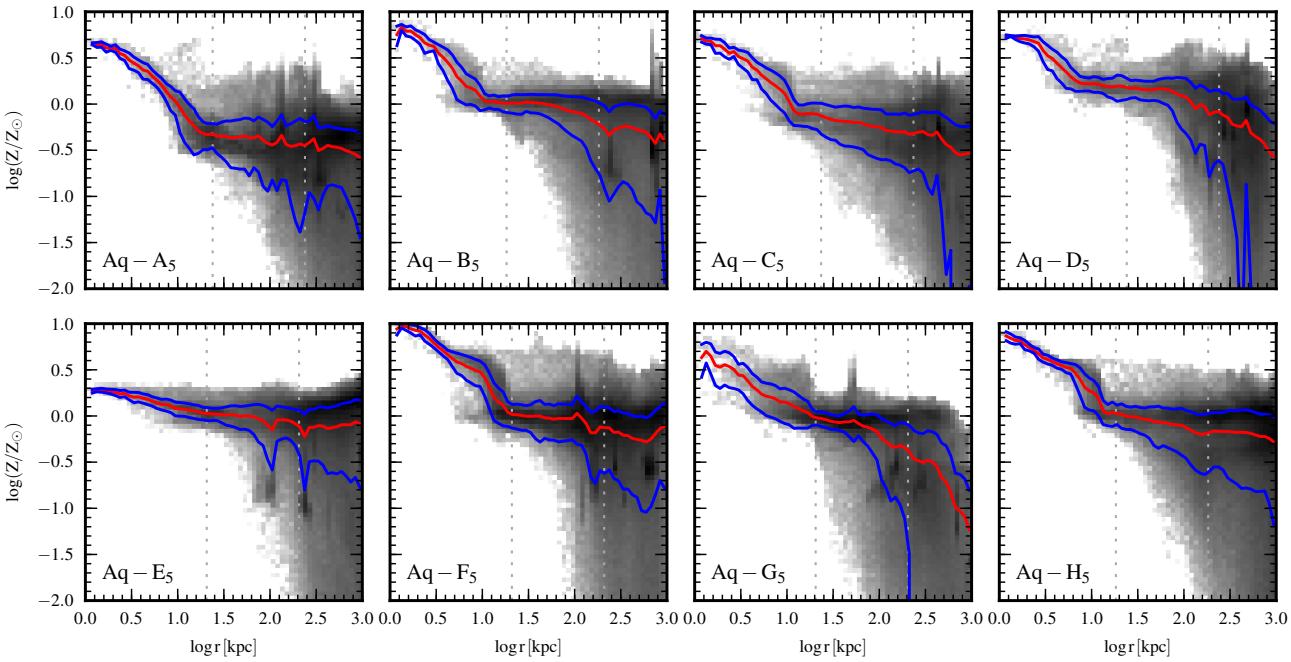

Figure 4. Metallicity distribution versus radial position of the diffuse gas phase for all the simulated haloes at $z = 0$. The figure shows a two-dimensional histogram built on 60×60 equally spaced logarithmic bins and weighted by the mass of gas cells so that the gray-scale encodes the gas mass present in each bin (darker colours indicate larger masses). The red solid lines in each panel represent the (mass-weighted) average gas metallicity as a function of the radius with the corresponding blue lines indicating the dispersion from the average value.

codes the gas mass present in each bin, with darker gray shades indicating larger values of the gas masses. In all the haloes the diffuse gas phase is substantially metal enriched. Inside the central galaxy (i.e. for radii below $0.1 \times R_{\rm vir}$) maximum metallicities of 3 up to ~ 10 times the solar value are not uncommon. Outside the galaxy and up to distances larger than the virial radius, the gas metallicity shows in general a rather flat trend with radius and the average mass-weighted metallicities, indicated by the solid red lines, are close to the solar value. The only exceptions are the Aq-A and Aq-C (and to a lesser extent the Aq-G) systems, which feature slightly sub-solar metallicities. The presence of a significant degree of metal enrichment in the haloes of our simulated galaxies demonstrates again the effectiveness of galactic winds in transferring metals from their production sites (the star-forming discs) to the circum-galactic regions surrounding them. The scatter in the metallicity distribution tends to increase with radius, as shown by the increasing width of the region around the average metallicity values delimited by the thin blue lines that indicate the dispersion around the average value. This implies that at any given radius, regions with rather different metallicity co-exist or, in other words, that metals are not homogeneously mixed in the gas. The bipolar nature of our galactic wind model (see also the right panel of Fig. 1) spontaneously leads to this type of behaviour because of its intrinsic anisotropy.

In Fig. 5 we present the phase diagram of the diffuse gas for all the simulated haloes at $z = 0$. Specifically, we built a two-dimensional histogram by dividing the $\log\ T - \log\ n$ plane in 80×120 equally spaced bins and plotting, as a gray-scale, the total gas mass inside each bin (darker gray shades are assigned to larger values of the mass). From Fig. 5, it is clear that the diffuse medium it is not uniformly distributed in the $\log\ T - \log\ n$ plane but gathers in two definite regions of the diagrams. One region is located at low densities ($10^{-5}{\rm cm}^{-3} < n < 10^{-3}{\rm cm}^{-3}$) and at temperatures $\log\ T > 5.5$ and centred on the halo virial temperature, which for the halo mass range that have been explored in these simulations is $\sim 10^6$ K. This warm-hot gas may be identified with the extended component of the CGM seen in the left and right panels of Fig. 1. The other region is at higher densities ($10^{-2}{\rm cm}^{-3} < n < 1\ {\rm cm}^{-3}$) and at an almost constant temperature of 10^4 K. This cold and relatively dense gas is closely related to the H I map presented in the central panel of Fig. 1 from which it can again be seen that this gas is found in the proximity of the central galaxy and its satellites and therefore has a less extended spatial distribution with respect to the warm-hot component. The transition between these two gas phases is not sharp but rather continuous. Indeed, the remaining part of the diagram in between the warm-hot and the cold dense gas is populated by an intermediate gas phase that can either result from the cooling of the denser and hotter fraction of the warm-hot phase via radiative losses – the less dense fraction can have a cooling time comparable or longer than a Hubble time – or the heating of the cold phase by the thermalization of the galactic wind energy or AGN feedback.

To quantify how the energy injected by the wind into the CGM affects the thermodynamic state of the latter, we show in Fig. 6 the spherically-averaged differential luminosity profiles of the diffuse gas together with the energy produced by stellar feedback that is available for galactic winds. Again, we split the contribution to the total gas luminosity between its cold, warm and hot phases. We derived the lu-

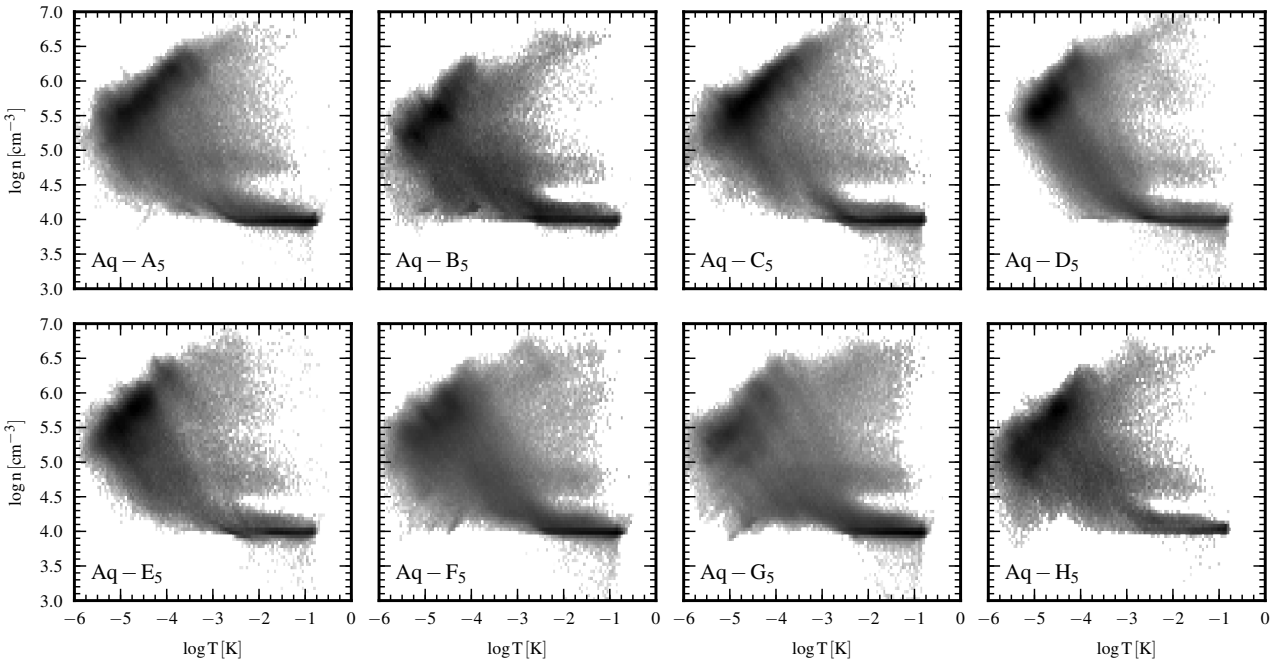

Figure 5. Phase diagram of the diffuse gas phase for all the simulated haloes at $z = 0$. The log T−log n plane is divided in 80×120 equally spaced bins on which a two-dimensional histogram is built. The histogram is weighted by the gas mass in each cell and the gray-scale encodes the amount of mass present in each bin (darker colours indicate larger values of the mass). It is readily apparent that the diffuse medium tends to concentrate in two distinct parts of these diagrams, one located towards high densities (10^{-2}cm$^{-3} < n < 1$ cm^{-3}) and low temperatures ($T \sim 10^4$K), and the other at low densities (10^{-5}cm$^{-3} < n < 10^{-3}$cm^{-3}) and temperatures close to the virial one ($\sim 10^6$ K).

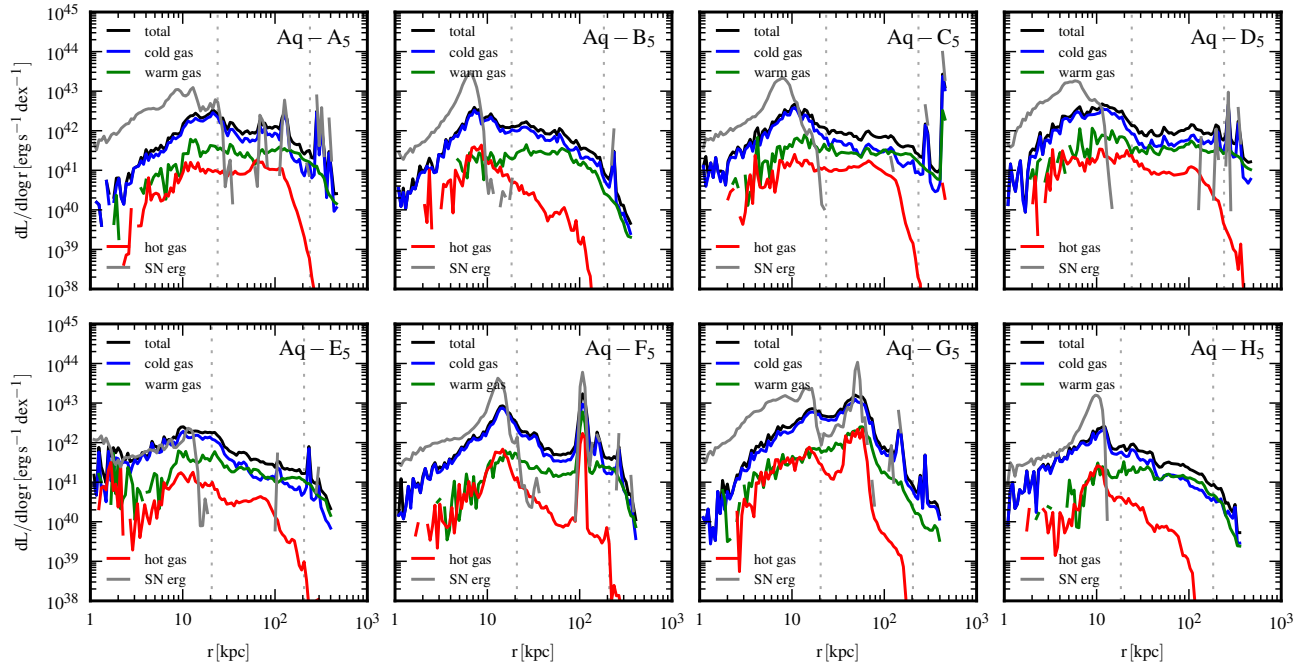

Figure 6. Spherically-averaged differential (bolometric) luminosity profiles for the diffuse gas phase for all the simulated haloes at $z = 0$, computed as the total cooling rate in equally logarithmically spaced radial bins divided by the bin width. The relative contributions of the cold, warm and hot components, selected according to the the gas temperature (see also Figs 2 and 3 above), are shown together with the energy of supernovae (gray lines) that is contained in galactic winds and ultimately deposited in the CGM of the simulated galaxies. Peaks in the latter quantity are usually found at the same locations of those of the total gas luminosity, suggesting that the energy carried by galactic winds is one of the major factors which sets the thermal state of the diffuse gas.

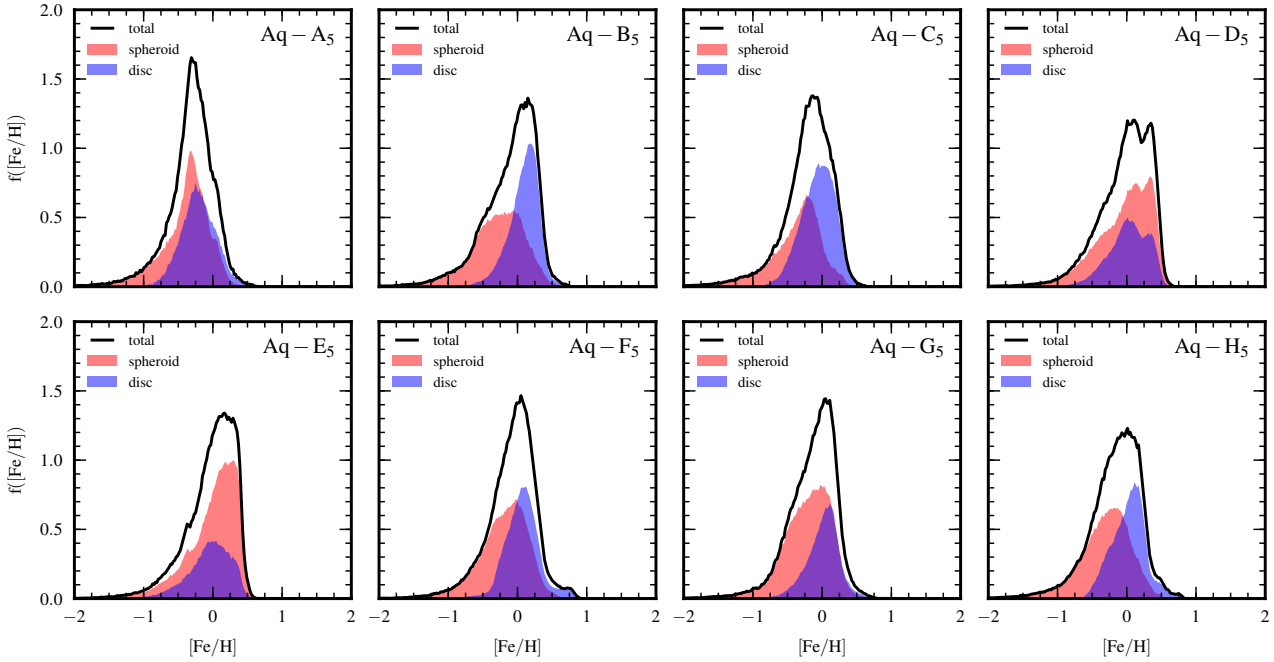

Figure 7. Histograms of the iron abundance relative to the solar value of stars within $0.1 \times R_{\rm vir}$ for all the simulated haloes at $z = 0$. The contributions of disc and bulge stars, separated according to their circularity parameter ϵ, are also shown. The histograms are normalized such that the area below them represents the stellar mass fraction in each component. Most of the histograms present a distribution of stellar metallicities peaked at around [Fe/H] ~ 0 and skewed towards sub-solar values. This general behaviour results from the superposition of the contributions of disc stars that are on average more metal-rich (because they are younger) and more narrowly distributed around the location of the peak of their metallicity distribution, and less metal-rich bulge stars that have a broader distribution with a tail towards lower metallicities.

minosity profiles by computing the total cooling rate of the gas (and thus the luminosities that we plot are *bolometric* luminosities) in 35 equally spaced logarithmic radial bins and then dividing the resulting rate by the bin width. The energy available to galactic winds is estimated by adding up the star formation rate (SFR) of star-forming gas cells within a given bin. This quantity is then converted into an energy rate by using a factor that expresses the supernova energy per unit mass for a Chabrier (2003) initial mass function times the assumed wind efficiency factor (for details see Vogelsberger et al. 2013, section 2.5.1). Also in this case the radial profile is obtained by dividing the supernova energy rate thus computed by the bin width.

Several important aspects can be appreciated from Fig. 6. Perhaps the most important one is that the energy in the galactic winds can easily compensate for the radiative losses of the gas, immediately suggesting that the wind energy is one of the major energy sources of the diffuse medium, if not the most prominent. Most of the wind energy is generated in the inner regions of the haloes, where the central galaxy is located and star formation is more vigorous. The supernovae rate suddenly drops at radii greater than ~ 20 kpc (roughly the size of the star-forming region) and so obviously does the wind energy, although occasional peaks of this quantity, very likely due to the presence of star-forming satellites, can be observed in the external regions. The presence of these peaks is very interesting because they are always accompanied by a corresponding peak in the gas luminosity. This further reinforces the idea that the energy contained in the galactic wind is an important source for powering the gas emission. Another key point is the fact that almost all of the gas luminosity is accounted for by the cold phase up to distances of ~ 100 kpc, where usually the warm phase gives a similar contribution. The hot phase is always sub-dominant in the luminosity budget. This is not surprising because gas in the cold and warm phases have temperatures that encompass the range where cooling is enhanced by the presence of metals (for solar metallicity, the cooling function peaks at a few $\times 10^5$ K). Furthermore, in the cold phase the enhancement due to the presence of metals is further assisted by a greater gas density. The hot phase lacks both of these boost factors: it has sufficiently high temperature to be located away from the peak of the cooling function – and actually at temperatures of $\sim 10^6$ K it is close to a *local minimum* of the cooling function before the cooling rate starts to increase again due to free-free emission – and its density is low, rarely exceeding a few 10^{-3} cm^{-3} and only in innermost regions (see Fig. 2).

3.2 Stellar metallicities

We now pass to analyse the metal content of stars comprising the central galaxy in our simulations to see how this is affected by strong galactic outflows. We first focus on the global metal content (Sec. 3.2.1) and we then discuss how the metal abundance varies as a function of the galactocentric radius (Sec. 3.2.2).

3.2.1 Global metallicity distribution

We start our analysis of stellar metallicity by presenting first its global distribution. We will focus on stars belonging to the central galaxy adopting our usual spatial cut that includes only stars inside $0.1 \times R_{\rm vir}$ of the host halo. Since the virial radii of all the simulated objects are ≈ 200 kpc, this spatial cut will include disc and bulge stars, as well as so-called halo stars (i.e., stars outside the disc of the central galaxy and gravitationally bound to it).

In Fig. 7, we show histograms of the iron distribution – a widely used proxy for the total metal content – relative to the solar value (taken from table 5 of Asplund et al. 2009) of such stars for all the simulated objects at $z = 0$. The histograms are normalised to the total stellar mass, and the contributions of disc (blue area) and bulge (red area) stars are also displayed. To separate these contributions we adopted the same kinematic criterion as in MPS14 based on the circularity parameter ϵ of stellar orbits, so that stars with $\epsilon > 0.7$ are considered as being part of a rotationally supported disc while the remaining part comprises the bulge. The total iron distribution has a peak at [Fe/H] ~ 0 in almost all the haloes. The only exception is Aq-A, where the peak of the distribution is shifted towards lower metallicities, giving [Fe/H] ~ -0.8. Usually, the iron distributions are unimodal and rather symmetric around their maximum value, although with a tail at sub-solar metallicities. Occasionally a second peak, as in the case of the Aq-D halo, or a small bump at super-solar metallicities, for instance in the Aq-F and Aq-H haloes, may be present.

The features of the total metallicity distributions are the result of the superposition of the distributions of disc and bulge stars that have quite different properties. Both distributions are unimodal (except again those of Aq-D) but they usually peak at different metallicities. For disc stars the peak is located at solar or slightly super-solar metallicities, while bulge stars are less metal-enriched and the peak of their distributions is located at sub-solar values. This is not surprising because the iron abundance (total metallicity) is a good tracer of the stellar age. Since disc stars are on average younger than bulge stars in this set of simulations (see MPS14), they form from a more metal-enriched interstellar medium, while older bulge stars are composed from more pristine material. However, not all the haloes feature peaks at two different locations. In particular, there are two exceptions, namely haloes Aq-D and Aq-E, where the metallicities of disc and bulge stars are very similar. It is interesting to notice that these two exceptions are also the two most bulge-dominated galaxies of our whole simulation set. Another distinctive difference between the metallicity histograms of disc and bulge stars is that the former are more narrowly distributed around their peak value, whilst the latter have a broader distribution and a significant tail at lower metallicities which is absent for disc stars. Due to the narrowness of the distribution, and also to the fact that most of these systems are disc-dominated, the peak of the distribution is usually more prominent for disc stars.

In Fig. 8, we present two-dimensional histograms of the [O/Fe] abundance versus the [Fe/H] abundance at $z = 0$ for all the simulated haloes. The histograms are generated by dividing the [O/Fe] − [Fe/H] plane into 80×300 equally spaced bins and computing the stellar mass falling into each bin. This quantity is encoded by the gray scale in Fig. 8, with darker gray shades assigned to larger masses. From stellar evolution theory an anti-correlation between the two abundances is expected. The strength of the anti-correlation (i.e., the slope in the diagram) is of course influenced by the details of the star formation history of the galaxy, but its origin lies mainly in the channels that are responsible for the production of oxygen (and the so-called α elements of which oxygen is the most abundant) and iron. Oxygen is mostly produced in core-collapse supernovae generated by the explosion of massive stars (> 8 M$_\odot$), while the main channel for iron production is represented by type Ia supernovae – thermonuclear explosions of white dwarfs. Because of the mass difference in the progenitors of these classes of objects, their explosion times are very different. In particular, core-collapse supernovae explode promptly, enriching the ISM rapidly with α elements, while type Ia supernovae need more time before they can start the iron enrichment. This implies that younger stars, that form from a more type Ia-enriched ISM and thus contain more iron, will have on average a small [O/Fe] ratio since there has been enough time for type Ia supernovae to efficiently enhance the abundance of iron with respect to the α elements. Given its origin, reproducing this anti-correlation is therefore an important test for the stellar evolution model and metal enrichment scheme employed in our simulation set.

From Fig. 8 it can be seen that at low metallicity (low values of [Fe/H]) there is significant scatter in the histograms, but this is reduced at higher metallicities ([Fe/H] > -0.5) where a well-defined sequence forms in all the panels. Most of the times the sequence is not unimodal but there is a hint of a gap located at [O/Fe] ~ 0.3. The declining trend of [O/Fe] with [Fe/H] is present in all the panels, but it is never very pronounced and tends to steepen, sometimes considerably, with increasing metallicity. Interestingly, in two of the haloes that show a double sequence, namely the Aq-B and the Aq-C haloes, the sequence with the higher value of [O/Fe] seems to show an inversion of the relation. A comparison with Milky Way data (red points) for halo, thick disc and thin disc stars[3] reveals, however, that the observed anti-correlation is much steeper than that present in our simulations. In particular, the oxygen abundance predicted by the simulations matches the observed values only in a narrow range of iron abundance between -0.5 and 0. At lower metallicities, some isolated histogram bins can reproduce the observed [O/Fe] ratios of the most metal-poor stars – we recall that data points are individual stellar measurements – but the bulk of the distribution has an oxygen abundance ~ 0.3 dex below the observed values. At higher metallicities, the discrepancy is more marked and our results are not able to capture the sharp cut-off in oxygen abundance observed at [Fe/H] ~ 0. The likely cause of this behaviour is either a slight over-production of oxygen in our simulations, or an underproduction if iron due to a too low SNIa rate, a question we further examine in Sec. 4.

[3] Observational data is a compilation from Gratton et al. (2003), Reddy et al. (2003), Cayrel et al. (2004), Bensby et al. (2005) and Ramya et al. (2012).

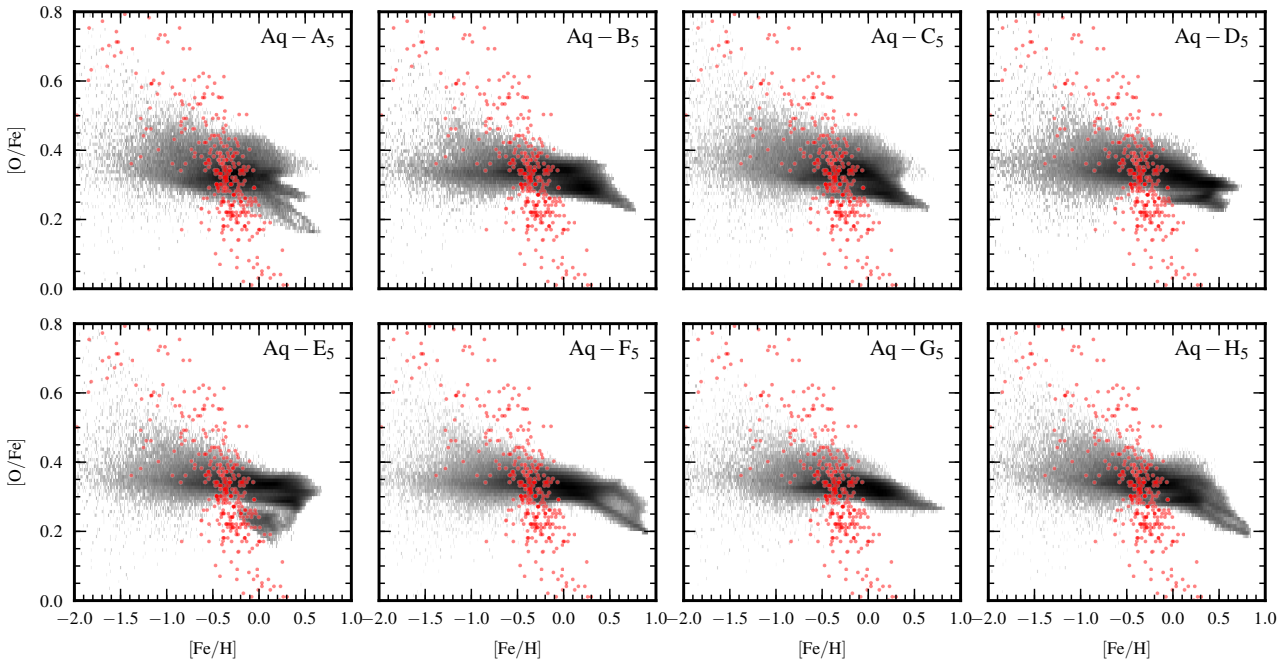

Figure 8. Oxygen versus iron abundance of stars within $0.1 \times R_{\rm vir}$ for all the simulated haloes at $z = 0$. The [O/Fe] − [Fe/H] plane is divided in 80×300 equally spaced bins on which a two-dimensional histogram is built. The histogram is weighted by the star particle mass and the gray-scale encodes the stellar mass present in each bin (darker colours indicate larger masses). In the [O/Fe] − [Fe/H] plane stars form a sequence that for increasing values of the iron abundance shows a slowly decreasing trend in the [O/Fe] values, although a substantial scatter is present. However, when compared to Milky Way data (red points) the trend is much flatter than the observed one. Especially at [Fe/H] ~ 0 our results are unable to reproduce the sharp cut-off in the [O/Fe] abundances present in the data.

3.2.2 Radial metallicity gradients

Since in the simulations the metallicity information of stars is available together with their positions, it is interesting to investigate how the (average) metallicity of the stellar component varies as a function of position. In particular, several observational surveys of the Milky Way disc (see Rudolph et al. 2006; CoşkunoğLu et al. 2012, and references therein) and of external spiral galaxies (e.g., Sanders et al. 2010; Barker et al. 2007; Magrini et al. 2009) report that the amount of metals is a decreasing function of the galactocentric distance of stars. It is therefore important to compare the predictions of our simulations with this observational fact.

We do this for the oxygen abundance in Fig. 9, where we present the average abundance profile of oxygen as a function of the galactocentric radius R for all the simulated haloes at $z = 0$. The abundance profile is derived by subdividing the radial range in 35 equally spaced bins and then by computing the total oxygen mass of the stars within a given bin divided by the total stellar mass in that bin. To use the same radial extent in all the panels, we have somewhat modified the spatial selection criterion for the stars, which are now included in the calculation only if they are inside a cylinder of radius 25 kpc that extends above and below the plane of the galactic disc for $0.1 \times R_{\rm vir}$. This distance is indicated in all the panels by the vertical gray dotted line. We also show, as gray points, the observed metallicities of 117 Galactic H II regions taken from Rudolph et al. (2006) together with two best-fitting relations derived by considering the sub-sample of sources whose metallicities are estimated through IR observations (solid gray line) or optical observations (long-dashed gray line). We recall that H II regions are kept ionised by the radiation of very young stars located at their centres, and therefore their metallicity is a reliable indicator of the metal content of the stars at their interior. In Fig. 9, we separately present the oxygen profiles for the total sample (black line), the disc (blue), and the bulge (red) stars. The separation in bulge and disc stars is performed based on the same criterion adopted in section 3.2.1.

By inspecting Fig. 9, one can immediately see that the oxygen abundance generally declines as a function of galactocentric radius in all the haloes. In agreement with the findings of Fig. 7, disc stars have an oxygen content always larger with respect to bulge stars. Since these plots show basically a mass-weighted metallicity, the oxygen abundance of the total sample lies in between the values for disc and bulge stars. Another important aspect is that the predicted values of the stellar oxygen abundance are compatible with the observations although, if one focuses on the total sample and on disc stars, it is at the upper end of what it is currently observed, especially at large galactocentric radii. This is presumably linked to the high [O/Fe] values at high stellar metallicities that have been discussed in Fig. 8 and again suggests that in our simulations the amount of oxygen may be mildly overproduced.

We noted earlier that the oxygen profiles are declining with radius; thus a metallicity gradient is present. For what concerns its strength, it is apparent from the comparison with the two best-fitting relations that in general the gradients predicted by our simulations are too shallow, even considering the optical fit to the data which has the least

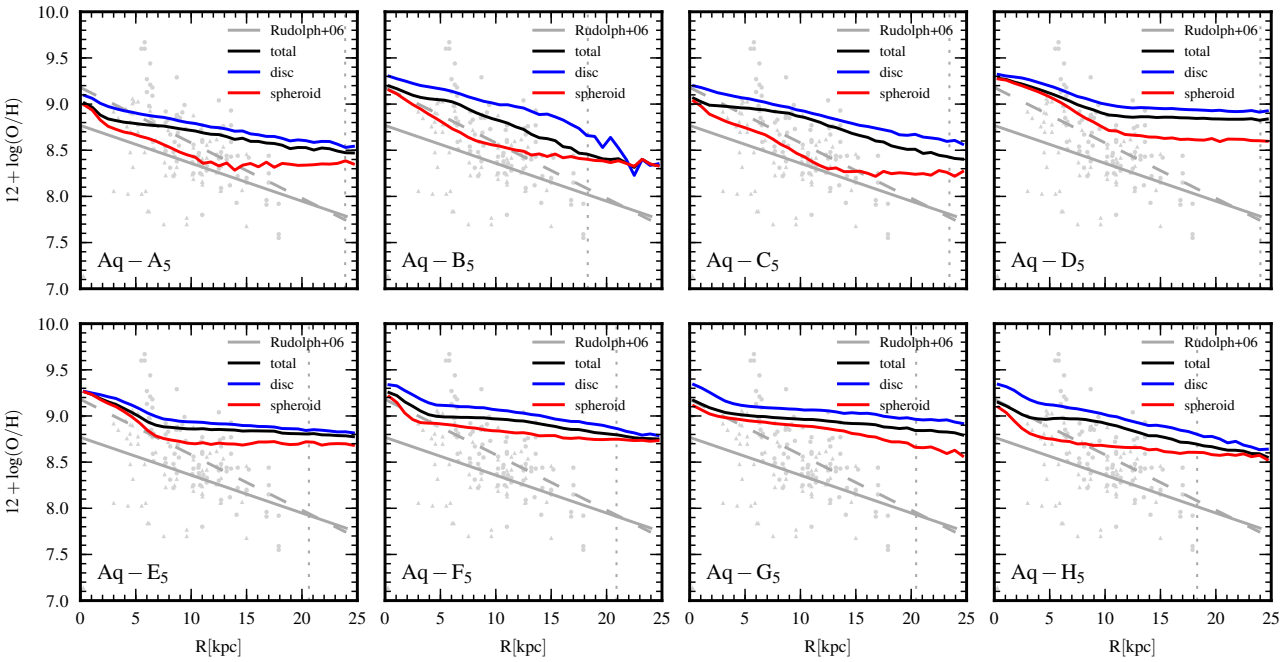

Figure 9. Stellar oxygen abundance as a function of galactocentric radius of star particles with $R < 25$ kpc and $|z| < 0.1 \times R_{\rm vir}$ for all the simulated haloes at $z = 0$. The plots show the radial abundance profiles in three different cases: the total sample of stars (black lines), the disc stars (blue lines) and bulge stars (red lines). Gray points are Milky Way data taken from Rudolph et al. (2006) with gray lines representing two different fits of the data in the case of IR derived metallicities (solid lines) or optical derived metallicities (long-dashed lines). The vertical dotted lines are located at $0.1 \times R_{\rm vir}$. The oxygen abundances predicted by the simulations are in agreement with the observed values and a metallicity gradient is clearly visible in all the panels for all the considered components, although it is always too shallow when compared to the observations.

pronounced slope. Only in two cases (Aq-B and Aq-C) the slope of the optical best-fitting relation is reproduced, but there is a considerable offset toward higher abundances, as previously discussed. In some of the haloes (Aq-A, Aq-B and Aq-C), bulge stars do a considerably better job in capturing the predicted metallicity trend, both in slope and normalisation. However, this does not constitute a fair comparison since H II regions surrounds newly formed stars in the Galactic disc and are not associated with bulge stars.

4 DISCUSSION

In the previous sections we have presented the main properties of the diffuse gas and stellar metallicity distributions that our simulations predict for galaxies similar to our own Milky Way. Here we extend the discussion on how these results compare to observations, examining in more detail which observational constraints are matched and where tensions between our simulations and the data lie.

We start with the properties of the diffuse gas surrounding the main galaxy. The picture that emerges from the simulations is that the structure of this gas component is strongly affected by galactic-scale winds, which in our simulations are necessary to curtail star formation. This is particularly evident if one compares the bipolar morphology (caused by the fact that the galactic wind is preferentially ejected perpendicularly to the star-forming disc in our current implementation) in the column density map of metals to the global morphology of the gas (see Fig. 1). The same comparison also shows that the diffuse gas is significantly metal-enriched out to and beyond the virial radius, and Fig. 4 backs up this conclusion. The average metal content in the diffuse gas is a slowly declining function of radius and, although a significant scatter is present, the average gas metallicity is very close to solar. This value is larger than that commonly inferred from observational constraints in the Milky Way other nearby galaxies, which seem to prefer a value closer to $\sim 0.1\,Z_{\odot}$ (Hodges-Kluck & Bregman 2013; Miller & Bregman 2013). However, due to its very low density, the metallicity of the diffuse gas phase and especially that of the hot emitting X-ray gas is poorly constrained. This metallicity is hence often simply either assumed or allowed to vary between $0.1 - 1\,Z_{\odot}$ (Anderson et al. 2013).

There is also another crucial factor that can substantially impact the degree to which the halo gas is enriched by metals. In our wind model, the metal loading of the wind can in principle be chosen *independently* from its mass loading. This was introduced to accomodate the fact that the mass loading is expected to arise in part through entrainment of gas with much lower metallicity than that of the star-forming gas itself. Indeed, it proved necessary in our wind model to allow galaxies to retain enough metals such that the observational relation between their stellar masses and metal content (see Fig. 13 in Vogelsberger et al. 2013) could be matched, while still efficiently expelling baryons to control star formation. The standard choice for our wind model is to load the outflow only with 40% of the metal mass contained in the parent gas cell. However, the results presented here suggest that even with this reduced metal loading our

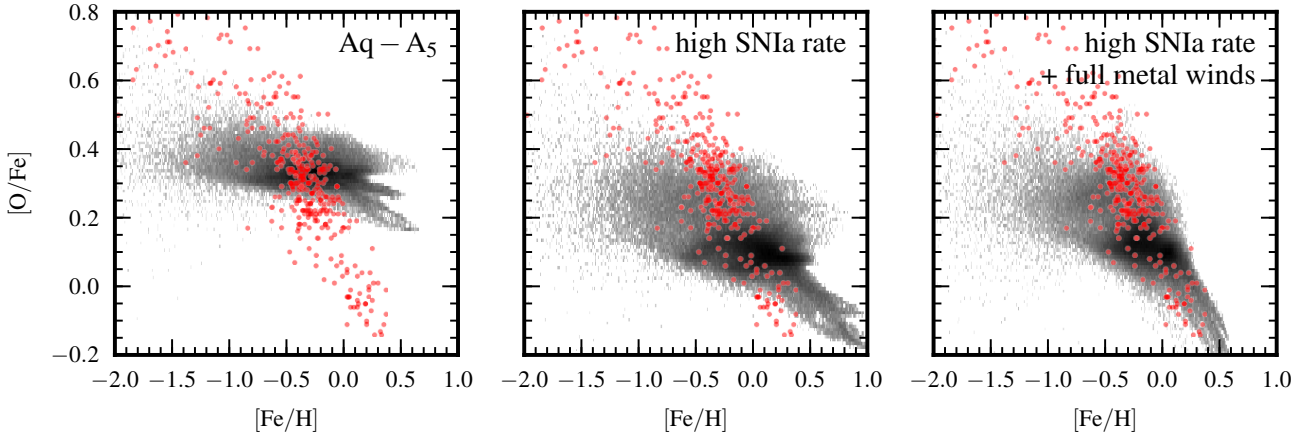

Figure 10. The same as Fig. 8 but showing the [O/Fe] − [Fe/H] plane for the Aq-A halo with three different parametrization of type Ia SNae and wind metal loading: our fiducial set-up (left panel), a simulation with an increased normalization (~ 4 times) in the time delay distribution of SNIa (middle panel) and a model that adds to the higher SNIa normalization fully metal-loaded winds. The increased SNIa rate in the middle and right panels results in a greater iron production that lowers the [O/Fe] values with respect to the fiducial case. Also, the anti-correlation between oxygen and iron content in the stellar component starts to emerge more clearly at high metallicities. In particular, the model that allows for fully metal-loaded outflows is now able to match the trend observed in the Milky Way.

galactic winds might be too efficient in transporting metals from galaxies to haloes.

Although the distribution of metals in the halo is in tension with what is observationally known, other properties of the diffuse gas such as density and mass distributions match Milky Way constraints quite well. The mass contained in the diffuse gas component is a substantial fraction of the total baryonic content of the halo (up to $\simeq 50\%$ of the universal baryon fraction), but in general the haloes are not baryonically closed (see table 1 in MPS14). The total densities are consistent with those needed to strip gas via ram pressure from dwarf spheroidal galaxies in the Milky Way (Gatto et al. 2013) and are compatible with X-ray emission upper limits and pulsar dispersion measures. We note that the last two constraints are traditionally seen as limits to the hot phase of the diffuse gas only (the so-called hot corona) and we caution the reader again that this phase is somewhat underrepresented in our simulations, except in haloes Aq-A and Aq-C.

The stellar metallicities in our simulations are able to capture the general trends expected in the Galaxy. For instance, the stellar iron content shows that disc stars are more metal rich and younger with respect to their bulge counterpart and the iron distribution peaks roughly at the solar value. However, when simulations are compared in more detail to the observations, discrepancies start to emerge.

A significant discrepancy is that our simulations have only a very weak dependence of the [O/Fe] abundance with respect to [Fe/H]. This relation is an important indicator of the relative contribution of core-collapse versus type Ia supernovae to metal enrichment. As such, it represents an important test of our stellar evolution module. In addition to the details of the star formation history in each halo, there are two major factors that can influence the [O/Fe]-[Fe/H] relation. The first is due to the uncertainties in the metal yields that we adopted in the model, which can induce an over- or under-production of one or several of the heavy elements (for instance of oxygen as mentioned in Sect. 3.2). The second is the time delay distribution of SNIa and its overall normalization relative to the core collapse rate, which dictates when iron will be released into the ISM and therefore can be incorporated into newly formed stars. All the simulations discussed in this paper were performed with the fiducial setup in Vogelsberger et al. (2013), but in principle it is possible to act on both factors to reconcile the simulation results with the observational constraints. Also, the efficiency with which metals are transported into the CGM by galactic winds (which in our model is regulated by their metal loading) can play a significant role.

We explore these issues in Fig. 10, where we present again the [O/Fe]-[Fe/H] relation for the Aq-A halo for three different models: our fiducial set-up (left panel), a simulation which uses a higher (~ 4 times) normalization of SNIa rate (middle panel) and a model that in addition to the higher SNIa rate allows for fully metal-loaded winds (right panel). The suggested increase in the normalization of the SNIa rate contains two factors, one is from changing the fiducial value of the model parameter from 1.3×10^{-3} (Maoz et al. 2012) to 2.5×10^{-3} [SN $\mathrm{M}_{\odot}^{-1}$], and another factor of about 2 arises from re-defining the SNIa rate parameter as the total number of SNIa per solar mass that explode in the stellar population over a Hubble time ($\simeq 13.56$ Gyr for this simulation set). In Vogelsberger et al. (2013), instead, the upper limit of the normalization integral for the SNIa delay time distribution was taken as infinite. Due to the shallowness of the adopted power law for the SNIa time delay distribution (the power law index is $s = -1.12$), there is then approximately a factor of 2 between these normalization conventions.

From Fig. 10 it can be seen that the increased number of SNIa events in the last two models leads to a higher iron production and therefore to smaller values of the [O/Fe] abundance. More interestingly, a clear anti-correlation between the iron and oxygen content starts to appear at the high-metallicity end. In particular, the model that allows for fully metal-loaded winds provides an impressively good match of the data for the Milky Way. We explicitly checked

that the models with increased SNIa rates yield consistent results for what concerns the galaxy properties examined in MPS14. We found no significant systematic differences except a somewhat higher SFR at late times (an expected trend due to the enhanced cooling of the gas caused by the slightly higher metal production of these simulations) that makes the galaxies appear slightly bluer than in our default run.

The other important mismatch between our simulations and the observations is the presence of only a shallow radial metallicity gradient in the stellar component. A possible explanation for this result is that our discs may suffer from an excessive radial migration of stellar orbits that can considerably reduce any preexisting radial metallicity gradient. An alternative explanation to be considered is that the material from which stars are born is too metal-rich. It is fairly well established by chemical evolution models of our Galaxy (e.g., Chiappini et al. 2001) that accretion of low-metallicity gas is needed to sustain its current SFR and to match its chemical signatures. In our simulations discs form in an inside-out fashion with gas accretion occurring preferentially at disc edges (see Figs. 9 and 10 in MPS14). In such a scenario, the accretion of relatively metal-poor material would naturally lead to a gradient in the star metallicities if radial migration of stars is not particularly strong. However, as we have discussed above, the material outside the disc has roughly solar metallicity and this similarity in chemical composition with the stellar component might cause a considerable flattening of the expected metallicity gradient.

5 SUMMARY AND CONCLUSIONS

In this paper, we have investigated the properties of the CGM and the relation between its metallicity and that of the stars comprising the central galaxy in eight cosmological 'zoom-in' simulations of Milky Way-sized haloes taken from the 'Aquarius' initial condition set. The simulations were performed with the moving-mesh code AREPO combined with a comprehensive model for galaxy formation physics, which includes, in addition to galactic winds, metal cooling, a self-consistent treatment of the stellar evolution and the associated mass and metal return to the gaseous phase, as well as AGN feedback. The simulations lead to the formation of realistic disc-dominated galaxies whose properties agree quite well with the scale relations and the observed features of late-type systems. The main findings of our analysis can be summarized as follows:

(i) galactic winds are the main channel for metal enrichment of the CGM as can be inferred from the bipolar morphology (induced by our wind model) of the distribution of the heavy elements in the halo;

(ii) the circum-galactic regions of all the simulated galaxies are substantially metal enriched by the winds out to and beyond the virial radius of the enclosing halo, with an average mass-weighted metallicity of $\sim Z_{\odot}$ and an almost flat trend with radius;

(iii) the density profile and the total mass of the diffuse circum-galactic gas are in agreement with Galactic observational constraints and the mass contained in this gas reservoir is a significant fraction of the baryon budget of the halo, although it is in general not sufficient to make the halo baryonically closed;

(iv) winds also alter the thermal state of the CGM and supply an energy input capable of sustaining its radiative losses;

(v) the global metallicity distribution of stars is in reasonable agreement with what is expected in the Milky Way and other star-forming galaxies, with disc stars being more metal rich than bulge stars and featuring a metallicity peak at about $Z_{\odot}$;

(vi) stars in the central galaxy exhibit a declining metallicity profile as a function of galactocentric radius, however this gradient is too weak when compared to Galactic observations;

(vii) the relation between oxygen over iron abundance and metallicity in the stellar component shows a trend which is too shallow with respect to Galactic observations; the oxygen vs iron abundance can be reconciled with observations by slightly changing the parameters describing the time delay distribution of SNIa events and the efficiency with which winds transport metals from the central galaxy to the CGM.

It is worth pointing out that the free parameters of our galaxy formation physics model, which are primarily those determining the strength of the galactic winds, were set to match the final stellar mass of the galaxy and not the properties of the diffuse circum-galactic gas and its metal enrichment properties. Therefore, the results listed above are genuine predictions of our galaxy formation model for these properties in late-type galaxies, which can thus be used to check the consistency of the model with constraints that are independent from those considered to set the parameters. The outcome of the analysis carried out in this work suggests that our model can satisfactorily predict the general properties of the circum-galactic medium associated with late-type systems and the metal content of stars contained within the central galaxy. However, in more detailed comparisons with the observations some discrepancies with the data start to emerge. These discrepancies are signaling deficiencies in our parameterization of the supernova type Ia rate, and possibly also in our phenomenological galactic wind implementation. Resolving these tensions in refined theoretical simulation models will be very helpful in further clarifying the connection between galaxies and their circum-galactic environment as well as for understanding the implications of this connection for galactic evolution.

ACKNOWLEDGEMENTS

We thank Andrea Gatto for making his routines to generate coronal profiles available to us and Lars Hernquist, Mark Vogelsberger and Till Sawala for useful discussions. FM and VS acknowledge support by the DFG Research Centre SFB-881 'The Milky Way System' through project A1. This work has also been supported by the European Research Council under ERC-StG grant EXAGAL-308037 and by the Klaus Tschira Foundation. Part of the simulations of this paper used the superMUC system at the Leibniz Computing Centre, Garching, under the project PR85JE of the Gauss Centre for Supercomputing, Germany.

REFERENCES

Abadi M. G., Navarro J. F., Steinmetz M., Eke V. R., 2003, ApJ, 591, 499

Agertz O., Teyssier R., Moore B., 2011, MNRAS, 410, 1391

Anderson M. E., Bregman J. N., Dai X., 2013, ApJ, 762, 106

Asplund M., Grevesse N., Sauval A. J., Scott P., 2009, ARA&A, 47, 481

Aumer M., White S. D. M., Naab T., Scannapieco C., 2013, MNRAS, 434, 3142

Balogh M. L., Pearce F. R., Bower R. G., Kay S. T., 2001, MNRAS, 326, 1228

Barker M. K., Sarajedini A., Geisler D., Harding P., Schommer R., 2007, AJ, 133, 1138

Battaglia G., Helmi A., Morrison H., Harding P., Olszewski E. W., Mateo M., Freeman K. C., Norris J., Shectman S. A., 2005, MNRAS, 364, 433

Bensby T., Feltzing S., Lundström I., Ilyin I., 2005, A&A, 433, 185

Boylan-Kolchin M., Bullock J. S., Sohn S. T., Besla G., van der Marel R. P., 2013, ApJ, 768, 140

Boylan-Kolchin M., Springel V., White S. D. M., Jenkins A., 2010, MNRAS, 406, 896

Boylan-Kolchin M., Springel V., White S. D. M., Jenkins A., Lemson G., 2009, MNRAS, 398, 1150

Brooks A. M., Solomon A. R., Governato F., McCleary J., MacArthur L. A., Brook C. B. A., Jonsson P., Quinn T. R., Wadsley J., 2011, ApJ, 728, 51

Cayrel R., Depagne E., Spite M., Hill V., Spite F., François P., Plez B., Beers T., Primas F., Andersen J., Barbuy B., Bonifacio P., Molaro P., Nordström B., 2004, A&A, 416, 1117

Chabrier G., 2003, ApJ, 586, L133

Chiappini C., Matteucci F., Romano D., 2001, ApJ, 554, 1044

CoşkunoğLu B., Ak S., Bilir S., Karaali S., Önal Ö., Yaz E., Gilmore G., Seabroke G. M., 2012, MNRAS, 419, 2844

Dehnen W., McLaughlin D. E., Sachania J., 2006, MNRAS, 369, 1688

Faucher-Giguère C.-A., Lidz A., Zaldarriaga M., Hernquist L., 2009, ApJ, 703, 1416

Gatto A., Fraternali F., Read J. I., Marinacci F., Lux H., Walch S., 2013, MNRAS, 433, 2749

Genel S., Vogelsberger M., Nelson D., Sijacki D., Springel V., Hernquist L., 2013, MNRAS, 435, 1426

Gratton R. G., Carretta E., Claudi R., Lucatello S., Barbieri M., 2003, A&A, 404, 187

Guedes J., Callegari S., Madau P., Mayer L., 2011, ApJ, 742, 76

Hodges-Kluck E. J., Bregman J. N., 2013, ApJ, 762, 12

Hopkins P. F., Keres D., Onorbe J., Faucher-Giguere C.-A., Quataert E., Murray N., Bullock J. S., 2013, ArXiv e-prints, 1311.2073

Hopkins P. F., Quataert E., Murray N., 2011, MNRAS, 417, 950

Lehner N., Howk J. C., Thom C., Fox A. J., Tumlinson J., Tripp T. M., Meiring J. D., 2012, MNRAS, 424, 2896

Li Y.-S., White S. D. M., 2008, MNRAS, 384, 1459

Magrini L., Stanghellini L., Villaver E., 2009, ApJ, 696, 729

Maoz D., Mannucci F., Brandt T. D., 2012, MNRAS, 426, 3282

Marinacci F., Binney J., Fraternali F., Nipoti C., Ciotti L., Londrillo P., 2010, MNRAS, 404, 1464

Marinacci F., Fraternali F., Nipoti C., Binney J., Ciotti L., Londrillo P., 2011, MNRAS, 415, 1534

Marinacci F., Pakmor R., Springel V., 2014, MNRAS, 437, 1750 (MPS14)

Martin C. L., Kobulnicky H. A., Heckman T. M., 2002, ApJ, 574, 663

Miller M. J., Bregman J. N., 2013, ApJ, 770, 118

Pakmor R., Marinacci F., Springel V., 2014, ApJ, 783, L20

Pakmor R., Springel V., 2013, MNRAS, 432, 176

Pettini M., Steidel C. C., Adelberger K. L., Dickinson M., Giavalisco M., 2000, ApJ, 528, 96

Prochaska J. X., Weiner B., Chen H.-W., Cooksey K. L., Mulchaey J. S., 2011, ApJS, 193, 28

Puchwein E., Springel V., 2013, MNRAS, 428, 2966

Rahmati A., Pawlik A. H., Raičevič M., Schaye J., 2013, MNRAS, 430, 2427

Ramya P., Reddy B. E., Lambert D. L., 2012, MNRAS, 425, 3188

Reddy B. E., Tomkin J., Lambert D. L., Allende Prieto C., 2003, MNRAS, 340, 304

Renaud F., Bournaud F., Emsellem E., Elmegreen B., Teyssier R., Alves J., Chapon D., Combes F., Dekel A., Gabor J., Hennebelle P., Kraljic K., 2013, MNRAS, 436, 1836

Rudolph A. L., Fich M., Bell G. R., Norsen T., Simpson J. P., Haas M. R., Erickson E. F., 2006, ApJS, 162, 346

Sakamoto T., Chiba M., Beers T. C., 2003, A&A, 397, 899

Sales L. V., Marinacci F., Springel V., Petkova M., 2014, MNRAS in press, ArXiv e-prints, 1310.7572

Sanders N., Caldwell N., McDowell J., 2010, in American Astronomical Society Meeting Abstracts #215 Vol. 36 of Bulletin of the American Astronomical Society, The Abundance Distribution In M31 From Optical Spectroscopy Of HII Regions And Planetary Nebulae. p. 415.33

Savage B. D., Sembach K. R., Wakker B. P., Richter P., Meade M., Jenkins E. B., Shull J. M., Moos H. W., Sonneborn G., 2003, ApJS, 146, 125

Scannapieco C., Tissera P. B., White S. D. M., Springel V., 2008, MNRAS, 389, 1137

Scannapieco C., Wadepuhl M., Parry O. H., Navarro J. F., Jenkins A., Springel V., Teyssier R., et al. 2012, MNRAS, 423, 1726

Scannapieco C., White S. D. M., Springel V., Tissera P. B., 2009, MNRAS, 396, 696

Sembach K. R., Wakker B. P., Savage B. D., Richter P., Meade M., Shull J. M., Jenkins E. B., Sonneborn G., Moos H. W., 2003, ApJS, 146, 165

Sijacki D., Vogelsberger M., Kereš D., Springel V., Hernquist L., 2012, MNRAS, 424, 2999

Soto K. T., Martin C. L., Prescott M. K. M., Armus L., 2012, ApJ, 757, 86

Springel V., 2005, MNRAS, 364, 1105

Springel V., 2010, MNRAS, 401, 791

Springel V., Di Matteo T., Hernquist L., 2005, MNRAS, 361, 776

Springel V., Hernquist L., 2003, MNRAS, 339, 289

Springel V., Wang J., Vogelsberger M., Ludlow A., Jenkins A., Helmi A., Navarro J. F., Frenk C. S., White S. D. M., 2008, MNRAS, 391, 1685

Springel V., White S. D. M., Jenkins A., Frenk C. S., Yoshida N., Gao L., Navarro J., Thacker R., Croton D., Helly J., Peacock J. A., Cole S., Thomas P., Couchman H., Evrard A., Colberg J., Pearce F., 2005, Nature, 435, 629

Stinson G. S., Bailin J., Couchman H., Wadsley J., Shen S., Nickerson S., Brook C., Quinn T., 2010, MNRAS, 408, 812

Stinson G. S., Brook C., Macciò A. V., Wadsley J., Quinn T. R., Couchman H. M. P., 2013, MNRAS, 428, 129

Stinson G. S., Brook C., Prochaska J. X., Hennawi J., Shen S., Wadsley J., Pontzen A., Couchman H. M. P., Quinn T., Macciò A. V., Gibson B. K., 2012, MNRAS, 425, 1270

Strickland D. K., Heckman T. M., Colbert E. J. M., Hoopes C. G., Weaver K. A., 2004, ApJ, 606, 829

Strickland D. K., Stevens I. R., 2000, MNRAS, 314, 511

Toro E. F., 1999, Riemann Solvers and Numerical Methods for Fluid Dynamics: A Practical Introduction. Springer-Verlag

Torrey P., Vogelsberger M., Genel S., Sijacki D., Springel V., Hernquist L., 2014, MNRAS, 438, 1985

Vogelsberger M., Genel S., Sijacki D., Torrey P., Springel V., Hernquist L., 2013, MNRAS, 436, 3031

Vogelsberger M., Sijacki D., Kereš D., Springel V., Hernquist L., 2012, MNRAS, 425, 3024

Xue X. X., Rix H. W., Zhao G., Re Fiorentin P., Naab T., Steinmetz M., van den Bosch F. C., Beers T. C., Lee Y. S., Bell E. F., Rockosi C., Yanny B., Newberg H., Wilhelm R., Kang X., Smith M. C., Schneider D. P., 2008, ApJ, 684, 1143